TUNL REU II

RESEARCH REPORT

31 MAY 2016 – 6 AUGUST 2016

Triangle Universities Nuclear Laboratory

Duke University
North Carolina State University
University of North Carolina at Chapel Hill

Box 90308, Durham, North Carolina 27708-0308, USA

The research described in this report is supported by the United States Department of Energy, Office of Science (Low Energy Nuclear Physics and Medium Energy Nuclear Physics Programs), under:

Grant No. DE-FG02-97ER41033 (Duke University),
Grant No. DE-FG02-97ER41042 (North Carolina State University), and
Grant No. DE-FG02-97ER41041 (University of North Carolina).

The TUNL Research Experiences for Undergraduates (REU) Program is supported by the National Science Foundation under:

Grant No. NSF-PHY-1461204.

Contents

Introduction **iv**

Personnel **v**

1 Research Based at Duke **1**

1.1 Numeric Digital Signal Processing Using a Slow Waveform Digitizer 2
1.2 Characterization of the Shielded Neutron Source at TUNL 4
1.3 Concept Study for Measuring Hadronic Parity Violation Through D(γ,n)p 6
1.4 Measurements of the ^{169}Tm(n,2n)^{168}Tm and ^{169}Tm(n,3n)^{167}Tm Cross Sections for the National Ignition Facility 8
1.5 Enge Feedback System 10
1.6 3D Printing of Radiation Detectors 12
1.7 Nuclear Data Evaluation for ^{15}F 14
1.8 Identification of the Neutral Current Interaction of Neutrinos in Liquid Argon Detectors . . . 16

2 Research Based at CERN **18**

2.1 First Measurement of Z+γ Production in 13-TeV Proton-Proton Collisions 19
2.2 Comparison of Fixed-R and Variable-R Jet Reclustering Using a 750 GeV Resonance 21

Introduction

An important national goal is to develop a diverse, internationally competitive, and globally engaged workforce in science and engineering. The Research Experiences for Undergraduates (REU) program is part of the effort to achieve that goal. The REU program at the Triangle Universities Nuclear Laboratory (TUNL) and Duke University provides a ten-week opportunity for undergraduate students to pursue research in the areas of nuclear and particle physics. This allows promising physics majors to broaden their education through participation in research at the frontiers of these exciting scientific fields.

In 2016, twelve students participated in the TUNL REU Program: eight spent the summer working on nuclear physics projects on the Duke campus, while the other four spent four weeks at Duke and six weeks at the European Center for Nuclear Research (CERN) near Geneva, Switzerland, working on particle physics projects. Having the nuclear and particle physics students in the same program facilitated cross-field intellectual exchange and the sharing of resources needed by both groups, while the participation of the Duke high energy physics group in the program gives it an international component.

Through introductory lectures and direct research involvement, the students gain experience and insights in the main stages of scientific research in nuclear and particle physics:

- The development of concepts to probe specific features of nuclear matter, particles and fields;
- The design, construction, testing, and installation of equipment and instrumentation;
- Data acquisition, analysis, and interpretation; and
- The dissemination of research results.

In addition to direct involvement in research projects, the REU program at Duke includes activities that are designed to broaden the students' physics foundation, enhance their research skills, and build confidence. These activities include: (1) regular meetings with the program coordinator, (2) research tutorials and special topic lectures, (3) a science writing tutorial, and (4) a required report and presentation by each student at the end of the program. The research reports written by the students form the main body of this document.

Personnel

2016 TUNL REU Participants

Student	*Home Institution*	*Faculty Advisor(s)*	*Class*
Ifeyani Achu	Southern Methodist Univ.	Mark Kruse	So
Adam Anthony	Juniata College	Mohammad Ahmed	Jr
Hannah Glaser	Virginia Tech	Ayana Arce	Jr
Spencer Griswold	Clarkson University	Ashutosh Kotwal	Jr
Chad Hobson	Lynchburg College	Calvin Howell & Werner Tornow	Jr
Alison (AJ) Roeth	University of Oklahoma	Kate Scholberg	So
Caitlin Seed	Boston College	Richard Longland	Jr
Jennifer Soter	Drew University	Megha Bhike & Werner Tornow	Jr
Emily Stump	Williams College	Al Goshaw	So
Thinh Truong	Lenoir-Rhyne University	John Kelley	Jr
Michael Wolff	Wooster College	Calvin Howell	Jr
Adele Zawada	Case Western Reserve	Phil Barbeau	Jr

2016 TUNL REU Administration

Principal Investigator:
Professor Calvin R. Howell

Co-Principal Investigator:
Professor Ayana Arce

Program Coordinator:
Dr. Alexander Crowell

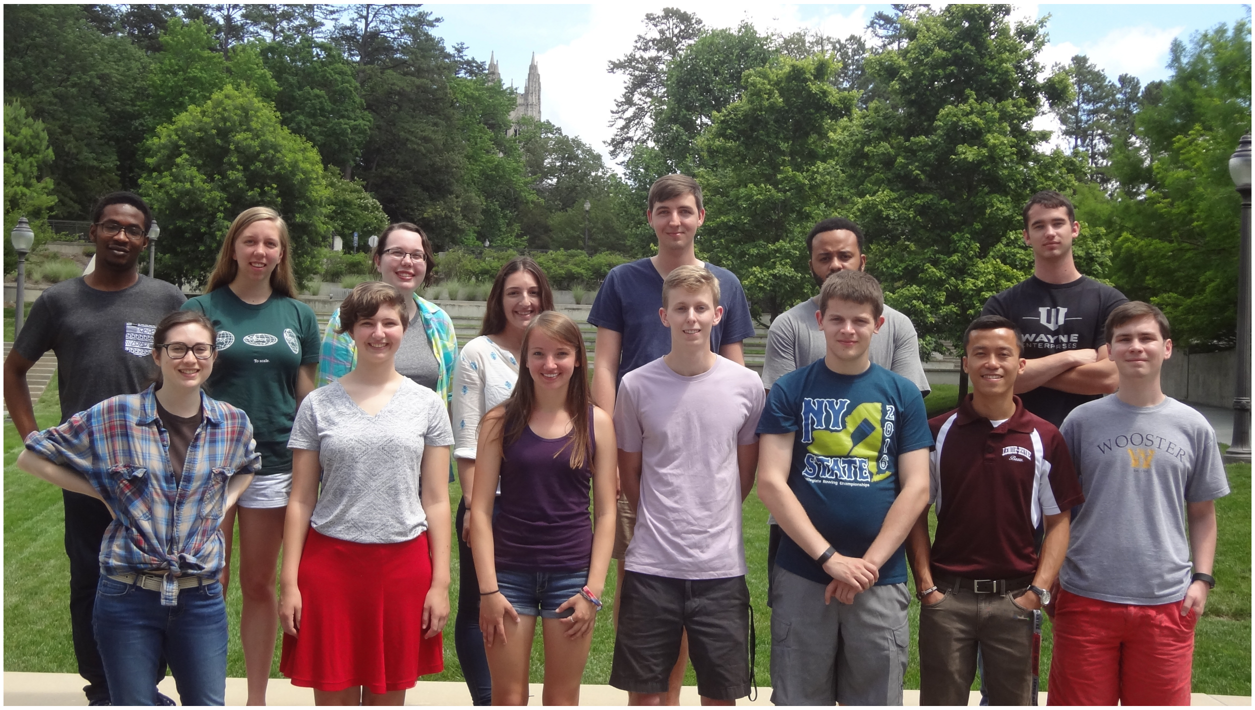

Participants in the TUNL Research Experiences for Undergraduates (REU) program are shown on the Duke campus. Shown in the photograph from left to right are: (front row) Hannah Glaser (Virginia Tech), AJ Roeth (University of Oklahoma), Adele Zawada (Case Western Reserve), Chad Hobson (Lynchburg College), Spencer Griswold (Clarkson University), Thinh Truong (Lenoir-Rhyne University), Michael Wolff (Wooster College); (back row) Ifeyani Achu (Southern Methodist University), Emily Stump (Williams College), Caitlin Seed (Boston College), Jenny Soter (Drew University), Adam Anthony (Juniata College), Abasi Brown[1] (North Carolina Central University),and John Wrights[1] (North Carolina A& T State University).

[1]Supported by funds outside of the NSF grant, but participated in many facets of the REU program.

Research Based at Duke

Chapter 1

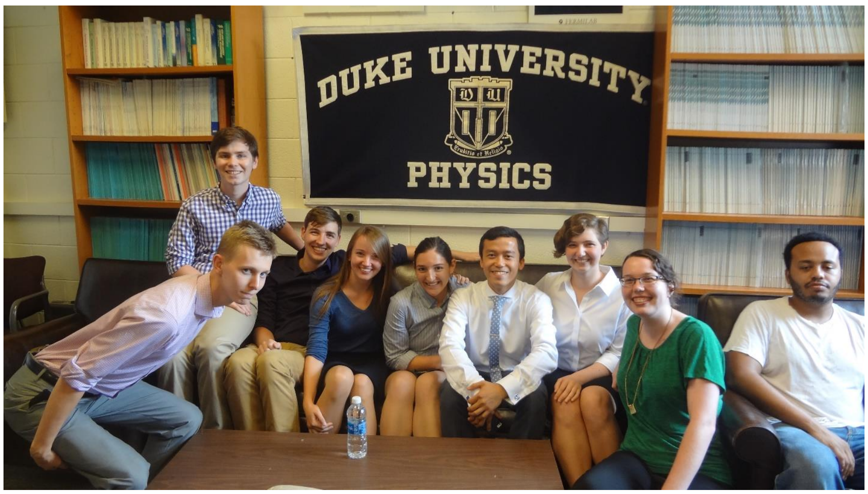

1.1 Numeric Digital Signal Processing Using a Slow Waveform Digitizer

A.K. Anthony, *Juniata College, Huntingdon, PA*; M.W. Ahmed, *TUNL*

Digital algorithms for timing filter amplification, constant fraction discrimination, trapezoidal pulse shaping, peak sensing with pileup rejection, and charge integration were developed and implemented. They are used with a 62.5 MS s^{-1} digitizer to calculate the energy resolution of the NaI detectors at HIγS. Peak sensing performed better than traditional charge to digital integration, but worse than the analog to digital data acquisition setup in use at HIγS.

Work is currently underway at HIγS to determine the electric, α_{E1}, and magnetic, β_{M1}, polarizabilities of nucleons. Polarizabilities are constants of proportionality between the induced dipole moments of composite electromagnetic systems and an externally applied field. The electric polarizability arises from a charge separation in the composite particle, while the magnetic polarizability is due to an alignment of the internal moments. Accurate measurements of both α_{E1} and β_{M1} would provide a test of quantum chromodynamics in the non-perturbative region. Using chiral effective field theory, one can extract the polarizabilities of protons and neutrons from the Compton scattering of high energy photons off hydrogen and deuterium targets, respectively. The polarizabilities of protons are well known; however, due to the experimental and theoretical difficulty in extracting neutron polarizabilities from deuterium scattering data, they are much less well determined.

Previous experiments at HIγS have looked at elastic scattering off deuterium, but have not had sufficient energy resolution to distinguish between the elastic and inelastic scattering peaks. With additional detectors on loan from the University of Kentucky, the next run should be able to distinguish between the two peaks. The new detectors require the digitization of an additional 32 channels, a task that the CAEN 1740 can achieve in a single board, greatly reducing the difficulty of synchronization with the existing data acquisition (DAQ) setup.

Work focused on characterizing the energy resolution achievable using the CAEN 1740 digitizer, which samples at a rate of 62.5 MS s^{-1}. The goal was to replicate or improve upon the energy resolutions currently being achieved at HIγS using an analog to digital (ADC) DAQ.

First, the current charge to digital method (QDC) used at HIγS was applied to a NaI detector whose output was passed though an amplifier and digitized by the CAEN 1740 without any additional analog signal processing.

The first few samples were averaged and used for a baseline correction to get a positive waveform, see Fig. 1.1, a requirement for both the QDC and trapezoidal shaping algorithms.

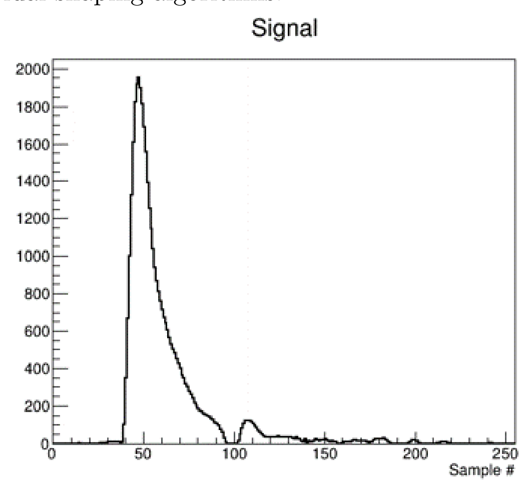

Figure 1.1: Typical NaI waveform.

An analog timing filter amplifier (TFA) was replicated digitally by taking the derivative of the baseline corrected waveform. This is used as the input to the digital constant fraction discrimination (CFD) algorithm, which duplicates the input signal, inverts and attenuates one of the copies, offsets the two by a user specified constant, and recombines the two signals. This produces a waveform that has a zero at the point the baseline corrected waveform starts rising. The zero of interest is found by taking the first zero crossing after some threshold. This zero is recorded as the start time of the signal and passed into the trapezoidal shaping and QDC algorithms.

The trapezoidal filtering algorithm used was based on one presented in Ref. [Jor94]. The recursive algorithm convolves the baseline corrected waveform with a trapezoidal shaping function to transform the waveform into a trapezoid [Jor94]. The algorithm assumes a discontinuous step up to the peak followed by an exponential decay. The actual signal produced by a NaI detector has a fairly significant rise time, enough to effect the output of the convolution. As seen in Fig. 1.2, rather than a true trapezoid the resulting shape has slight curves to the edges and the flat top has local maxima at the edges and a local minimum around the center.

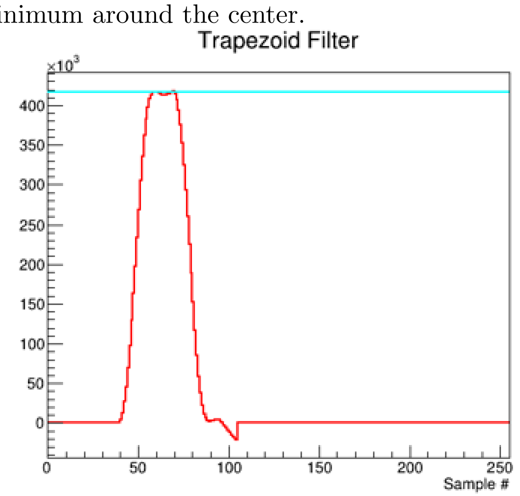

Figure 1.2: Trapezoid of a typical waveform. The top flat line indicates the peak detection.

From the transformed signal, the energy of the particle is extracted. Like the area under the baseline corrected curve, the height of the trapezoid is proportional to the amount of energy deposited in the detector during the event window. This method is known as digital ADC. Because the digital ADC method is less susceptible to noise from ballistic effects and charge trapping when the pulse length is short, as is the case in NaI detectors, it is expected that the filter method will be more accurate than QDC.

One can extract the location of the flat top from the second derivative of the trapezoid, which is characterized by a sharp negative spike. When pile-up occurs, multiple particles are detected in the same event window and there is a distinct change in the slope of the rising edge as shown in Fig. 1.3. This change in slope is characterized by a spike in the second derivative. By counting the number of times the second derivative spikes before the flat top, which is detectable by a large negative spike in the second derivative, pile up events can be identified and discarded.

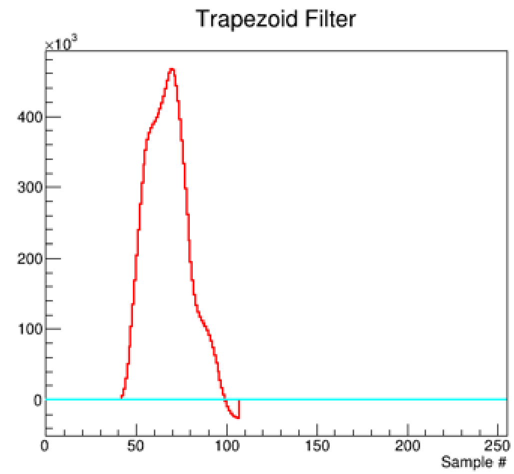

Figure 1.3: Trapezoid of a pile-up waveform. The change in slope of the rising edge is clear. The flat-line indicates the baseline.

The energy resolution of a NaI detector at the 4.4 MeV γ-ray peak from an AmBe source was found using QDC, analog ADC, and digital ADC. The resolution was calculated by performing a Gaussian curve fit of the energy peak and taking the Full-Width Half Max (FWHM) value at the mean energy of the peak. The results are shown below in Table 1.1.

Table 1.1: Energy Resolution at 4.4 MeV

Method	FWHM (keV)	Resolution (%)
Analog ADC	202	4.56
Digital ADC	216	4.89
QDC	288	6.49

Analog ADC performed the best out of the three methods as expected, but digital ADC performed much better than traditional QDC methods.

[Jor94] V. T. Jordanov and G. T. Knoll, Nucl. Instrum. Methods A, **345**, 337 (1994).

1.2 Characterization of the Shielded Neutron Source at TUNL

C.M. Hobson, *Lynchburg College, Lynchburg, VA*; S.W. Finch, C.R. Howell, R.C. Malone, W. Tornow, *TUNL*

Neutrons are produced at the shielded neutron source (SNS) via the ^{2}H(d,n)^{3}He reaction and then collimated by heavy shielding to form a beam. Our work was performed to provide researchers who use the SNS with the beam parameters necessary to plan and conduct an experiment. We present results on the position and size of neutron beam as well as on the structure and magnitude of the neutron and γ-ray backgrounds.

The shielded neutron source (SNS) located in the Tandem Laboratory at TUNL was rebuilt in 2015 and provides a well-collimated monoenergetic neutron beam. A circular or rectangular double-truncated conical copper collimator can be used to provide the necessary beam shape. Researchers have an interest in using this space for experiments ranging from neutron-deuteron breakup measurements to calibrating new detectors. When planning an experiment at the SNS, it is crucial to understand the backgrounds associated with the beam as well as the beam's size, position, and intensity. Our work aims to measure the beam parameters necessary to plan and execute an experiment at the SNS.

To measure the neutron beam profile, neutrons were produced via the ^{2}H(d,n)^{3}He reaction with a pulsed deuteron beam (period = 400 ns, FWHM = 2 ns). Beam profiles were measured for neutron energies of 5 and 10 MeV using the circular collimator and at energies of 10 and 16 MeV using the rectangular collimator. We performed beam scans at 1.72 m and 2.43 m from the center of the gas cell. We used a paddle detector to normalize our data and rectangular plastic scintillators to scan the beam. The widths of the scintillators were 3.5 mm at 1.72 m and 9.4 mm at 2.43 m to increase the count rate. Sample results are shown in Fig. 1.4. The number of neutrons detected inside the beam was roughly three orders of magnitude larger than outside the beam. For all configurations, we found the beam axis to be angled beam left and upward from the optical zero-degree axis. These angles ranged from 0.22° to 0.89°. Previous scans suggest the position and angle of the beam axis is sensitive to the beam tune [Mal15].

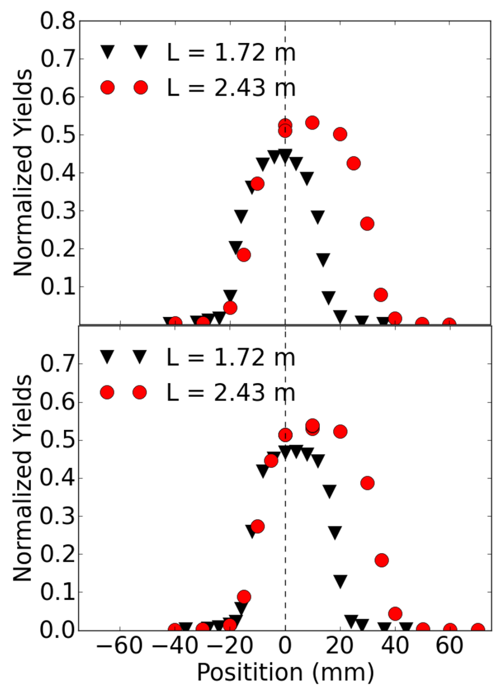

Figure 1.4: Beam scans at 10 MeV with the circular collimator. The variable L represents the distance to the gas cell. The top (bottom) figure is a horizontal (vertical) scan where a positive distance is beam left (up). The dotted line represents the optical center point.

Our experimental setup for measuring relevant backgrounds is shown in Fig. 1.5. It featured five 2 in. x 2 in. cylindrical BC501A liquid scintillators, one centered on the optical zero-degree axis and two each at angles of 35° and 75° mirrored over the optical zero-degree axis. The latter four were 0.75 m from the scattering sample. The scattering sample was a graphite cylinder 28.6 mm in diameter and 38 mm high, placed 1.64 m from the center of the gas cell. Backgrounds were measured at neutron energies of 10 and 16 MeV.

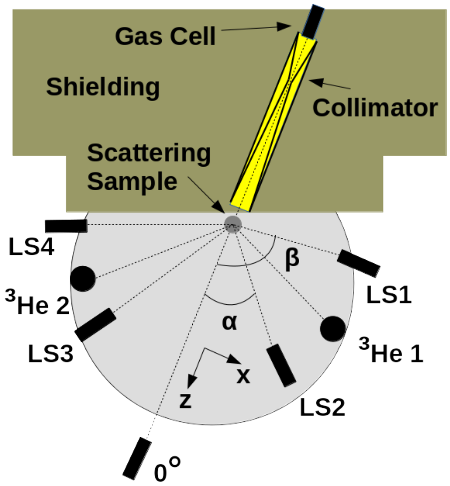

Figure 1.5: Overhead view of our experimental setup (not to scale). The angles are $\alpha \approx 75°$ and $\beta \approx 35°$.

Although we focused on neutron backgrounds, roughly 80% of the counts in the detectors were due to time-uncorrelated γ rays. The first neutron background that we identified was neutrons that traveled directly from the gas cell to the detectors. Due to the angle of the collimator, there is less shielding along a straight line between the gas cell and detectors on the beam left side of the table than detectors on the beam right side of the table (see Fig. 1.5). Specifically, there is about 0.5 m more shielding between the gas cell and LS4 than LS1. Time-of-flight spectra for LS1 showed a peak corresponding to neutrons traveling directly from the gas cell to the detector that was not present in the spectrum for LS4.

Table 1.2: Minimum neutron scattering cross section times moles of scattering sample

Detector	Beam Energy (MeV)	$\sigma \cdot n$ (mb mol)
LS1	10	5.7
LS2	10	42.4
LS3	10	30.7
LS4	10	2.6
LS1	16	27.9
LS2	16	62.1
LS3	16	31.0
LS4	16	6.1

To quantify measurement sensitivity, we integrated the neutron-carbon elastic scattering peak in the neutron time-of-flight spectrum for each detector and for runs with the graphite sample both in and out of the beam. After normalizing sample-in and sample-out runs by the integrated beam current, we subtracted the background to determine the ratio of background neutrons to elastically scattered neutrons. With this ratio, we could determine the minimum product of scattering cross section and moles of sample necessary to achieve a net count-to-background ratio of at least one. Table 1.2 displays our results.

We also quantified the ratio of fast and thermal background neutrons to monoenergetic neutrons in the beam. Our parameter of interest was the number of background neutrons per detector volume per monoenergetic neutron. This allows a research group to predict the background for a given detector and run time. Table 1.2 shows our results for thermal neutrons. To obtain these results, we moved a 30 cm long ^{3}He ionization tube with a diameter of 1.75 cm around the table in the SNS during our 16 MeV runs. For our detector, we measured about one thermal background neutron for every 26 monoenergetic neutrons. We also determined that the thermal neutron background is independent of location.

Table 1.3: Thermal neutrons (N) per detector volume per total neutrons (N_t) detected at various locations corresponding to a scattering angle of θ. The scattering sample is positioned at (0,0,0).

Position (x,y,z) (cm)	θ	$N V^{-1} N_t^{-1}$ (cm^{-3})
(26.04, -20.00, 95.25)	15.3°	7.37E-4
(36.20, -20.00, 36.83)	44.5°	5.06E-4
(22.86, -20.00, -5.08)	77.5°	5.70E-4
(-33.02, -20.00, 91.44)	−19.9°	4.85E-4
(-38.10, -20.00, 36.86)	−46.0°	3.72E-4
(21.59, -20.00, 96.52)	12.6°	6.32E-4
(21.59, 16.83, 96.52)	12.6°	5.60E-4

Similarly, we calculated the fast background neutrons per detector volume per monoenergetic neutron in the beam for regions in the time-of-flight spectra for each liquid scintillator at 10 MeV and 16 MeV. We found these to be dependent on both the energy of the beam and the position of the detector. For the elastic scattering peak at 16 MeV, the number of fast background neutrons per monoenergetic neutron in the beam ranged from 1,743 for LS2 to 19,095 for LS4.

[Mal15] R. C. Malone *et al.*, TUNL Progress Report, **LIII**, 12 (2015).

1.3 Concept Study for Measuring Hadronic Parity Violation Through D(γ,n)p

M.S. Wolff, *The College of Wooster, Woooster, OH*; C.R. Howell, *TUNL*

This project is part of the design of an experiment measuring the parity non-conserving (PNC) asymmetry in the D(γ,n)p reaction using an upgraded HIγS2 facility. After designing an initial detector geometry, a code was written to find limits for approximate instrumental asymmetry. The code will also be able to perform further simulations for modified detector geometries.

It is currently unknown whether measurements of interactions between low energy nucleons are consistent with the Standard Model. There have been many measurements of such interactions involving heavy nuclei, but their strong interactions are not fully understood in terms of QCD. Thus the measurement of parity-violation (PV) reactions in very light nuclei, whose strong interactions are well understood, is an important avenue to isolate and investigate the contribution of the weak force to low-energy nucleon reactions.

In the meson exchange model developed by Deplanques, Donoghue, and Holstein [Des80], the hadronic PV potential is described in terms of nucleon-nucleon couplings based on the exchange $\pi^{\pm}$, ρ, and ω mesons, with one weak vertex and one strong vertex.

The present experiment aims to investigate the PV asymmetries within the photodisintegration of deuterium, where γ rays cause a deuterium nucleus to break into a proton and neutron, the latter having an energy of less than 300 keV. In this experiment, the PV asymmetry after flipping the helicity of the γ-ray beam is on the order of 10^{-7}. Thus we are seeking an uncertainty of 10^{-8} in our measurements, which, in turn, requires the detection of 10^{16} reactions. Unfortunately, given the current HγGS flux of about 10^{6} photons per second for 2.3 MeV circularly polarized photons [HIG10], this experiment would need to run for thousands of years at to reach the desired number of events. The proposed facility upgrade to HγIGS2 would provide a beam flux several orders of magnitude higher than what is currently achievable and would allow the experiment to run over the course of about a year while still achieving the desired 10^{16} observed reactions.

The design of the detector to be used in this experiment is based on the INVS IV detector [Arn11] and is shown in Fig. 1.6. The main polyethylene body of this cylindrical detector, houses thirty-six helium gas ionization tubes. It is 40 cm in diameter and 46 cm in length, with an inner radius of 17 cm. Alternating helium-3 and helium-4 gas ionization tubes are placed in two radially symmetric rows. The former count neutrons, while the helium-4 tubes provide a measure of the γ-ray background.

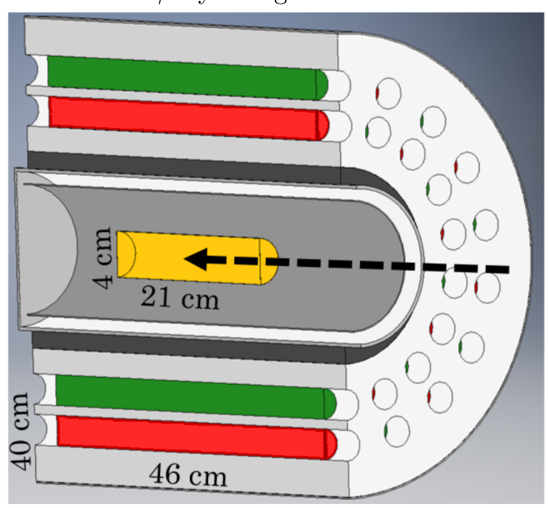

Figure 1.6: A cross-section of the initial detector and target design, showing the γ beam path as it hits the liquid deuterium target.

The liquid deuterium target is placed at the center of the detector. It is contained within a vacuum and protected by a radiation shield. The cylindrical target has internal dimensions of 21 cm in length and 4 cm in diameter and is housed in 0.01 cm thick Kapton. Between the target and detector, a 1.5 cm thick graphite moderator lowers ejected neutrons to thermal level before they reach the body of the detector.

We are currently in the process of iteratively modifying the design and simulating the relative efficiency and instrumental asymmetries of a proposed trial geometry of the detector. Further iterations of the design will be altered to minimize sources of instrumental asymmetry associated with any changes in the γ-ray beam after its helicity has been flipped. Three possible sources of such instrumental asymmetry are changes in the beam density profile, changes in the position of the beam, and changes in the angle of incidence. The numerical approximations detailed in this progress report focused on the latter two effects. To keep data consistent between runs, it is necessary that any changes in relative detection efficiency due to a helicity flip must be less than one part in 10^{-7}.

Simplifying the geometry of the detector, the Mathematica code approximates the γ-ray beam's path through the target as five points in a line. The line can be altered to simulate either translating the beam laterally, or changing the entry angle to study sensitivity to these changes. Using the five points in the line as reaction locations, the code finds the relative detection efficiency of the detector, ε_{eff}. This quantity is a function of the length of a particle's path through the detector, r, and is calculated as

$$\varepsilon_{\text{eff}}(r) = a\left(1 - e^{-r/137}\right). \tag{1.1}$$

The path length factor of 137 is an approximation of detection efficiency based on data collected with the INVS IV detector. By integrating over all possible paths a reaction particle may take, we determined the relative efficiency of the detector given a specified beam configuration.

After running the code over small lateral and angular displacements, the changes in relative detection efficiency as a function of beam displacement were found to fit well to quadratic functions, as shown in Fig. 1.7. Solving these functions for changes in efficiency on the order of 10^{-7}, it was found that the maximum viable lateral displacement is about 60 μm from center, and the maximum viable angular displacement is 350 μrad, corresponding to an exit point 73 μm from the center of the target.

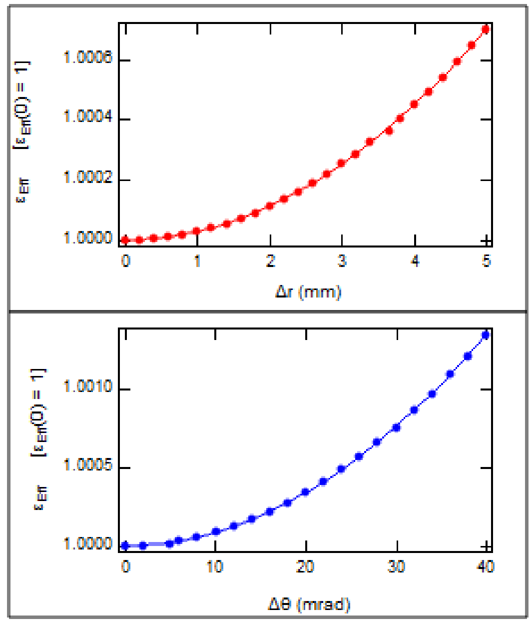

Figure 1.7: Relative efficiency plotted against lateral and angular displacement. Results are normalized such that $\varepsilon_{\text{eff}} = 1$ for a centered beam.

Because this simulation treats the γ-ray beam as a one-dimensional line, these values are especially restrictive, as similar displacements would not affect the profile of a beam with finite volume as severely.

For future work, the Mathematica code is also able to alter the detector dimensions for optimization of the geometry.

[Arn11] C. W. Arnold *et al.*, Nucl. Instrum. Methods A, **647**, 55 (2011).

[Des80] B. Desplanques, J. F. Donoghue, and B. R. Holstein, Ann. Phys., **124**, 449 (1980).

[HIG10] *HIγS Flux Performance Table (v2.3)*, `http://www.tunl.duke.edu/documents/public/HIGSBeamParameters.pdf`, 2010.

1.4 Measurements of the ^{169}Tm(n,2n)^{168}Tm and ^{169}Tm(n,3n)^{167}Tm Cross Sections for the National Ignition Facility

J. Soter, *Drew University, Madison, New Jersey*; Krishichayan, M. Bhike, W. Tornow, S.W. Finch, *TUNL*

Measurements of the ^{169}Tm(n,2n)^{168}Tm and ^{169}Tm(n,3n)^{167} cross section have been performed for neutron energies ranging from 9.0 to 20.6 MeV using the neutron activation technique. De-excitation γ rays were recorded off-line with high-purity germanium detectors in TUNL's low-background counting facility. Our results provide the basis for investigating properties of the inertial confinement fusion plasma in deuterium-tritium capsules at the National Ignition Facility.

^{169}Tm(n,2n)^{168}Tm and ^{169}Tm(n,3n)^{167}Tm cross-section measurements have recently been carried out to obtain information on the density of the plasma created in inertial confinement fusion at the National Ignition Facility (NIF). In the current literature data for ^{169}Tm(n,2n)^{168}Tm, there are up to 50% discrepancies between the different evaluations, and few measurements have been carried out near the threshold. Furthermore, no single group has measured the full cross section of the ^{169}Tm(n,2n)^{168}Tm reaction. The goal of this experiment is to resolve the discrepancies and extend the measurements to lower energies with special emphasis on the 9 to 15 MeV energy region for the ^{169}Tm(n,2n)^{168}Tm reaction, as well as energies ranging from 17 to 20.6 MeV for the ^{169}Tm(n,3n)^{167}Tm reaction.

The experiment was performed at TUNL via the neutron activation technique [Bhi14]. The targets were thulium disks 1.1 cm in diameter. To monitor the neutron flux, gold and zirconium foils of the same area were attached to the front and back sides of the target. Monoenergetic neutrons were produced at energies ranging from 9 to 14 MeV in 0.5 MeV increments using the ^{2}H(d,n)^{3}He reaction. For energies greater than 14 MeV, the ^{3}H(d,n)^{4}He neutron source reaction was utilized to produce monoenergetic neutrons. As shown in Fig. 1.8, the experimental setup for the measurements using the ^{2}H(d,n)^{3}He reaction consists of a 3-cm-long gas cell pressurized to 3 atm with high-purity deuterium gas. A 6.5 micrometer Havar foil separates the gas from the accelerator vacuum. The thulium targets and monitor foils were placed 2.5 cm from the neutron production point. The set up for the ^{3}H(d,n)^{4}He production reaction was similar, except a tritiated titanium layer was used in place of the gas cell.

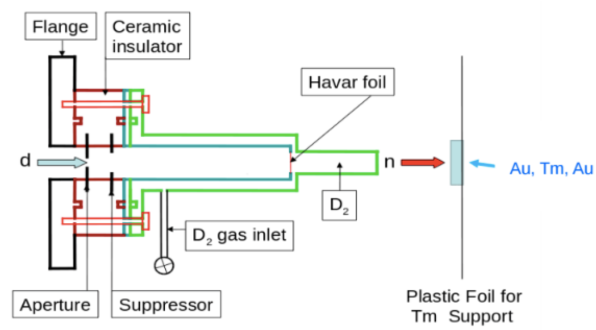

Figure 1.8: Schematic view of the experimental arrangement using the ^{2}H(d,n)^{3}He reaction.

After five hours of irradiation, the de-excitation γ rays from the first excited states of ^{168}Tm and ^{167}Tm were recorded off-line using well-shielded and calibrated high-purity germanium (HPGe) detectors of 30%, 55%, and 60% relative efficiency in TUNL's low-background counting facility. Sample and monitor foils were placed in acrylic holders and positioned 5 cm away from the face of the detector. Table 1.4 summarizes the properties of the γ-ray transitions of interest.

Cross sections were calculated using the well-known activation formula at 15 different energies for the ^{169}Tm(n,2n)^{168}Tm reaction using the four most intense peaks. Our results are plotted in Fig. 1.9. The cross-section values are in the range of 0.5 to 2 b. The cross section increases rapidly around 9 MeV, reaching saturation at just under 2 b for incident neutrons of 11 to 14.8 MeV, consistent with the measurements of Frehaut *et al.* [Fre80]. At higher energies,

Table 1.4: Properties of the γ-ray transitions used for the ^{169}Tm(n,2n)^{168}Tm and ^{169}Tm(n,3n)^{167}Tm reactions and monitor reactions.

Nucleus	Isotopic Abundance	$T_{1/2}$	Threshold (MeV)	E_x (keV)	I_γ (%)
^{169}Tm(n,2n)^{168}Tm	100%	93.1(2) d	8.082	184.295 (2)	18.15 (16)
				198.251 (2)	54.49 (16)
				447.515 (3)	23.98 (11)
				815.989 (5)	50.95 (16)
^{169}Tm(n,3n)^{167}Tm	100%	9.25 (2) d	14.963	207.801 (5)	42 (8)
^{197}Au(n,2n)^{196}Au	100%	6.1669 (6) d	8.114	355.73 (5)	87
^{90}Zr(n,2n)^{89}Zr	51.45%	78.41 (12) h	12.103	909.15 (15)	99.04

the values decrease consistent with the measurements carried out by Vesser *et al.* [Vee77].

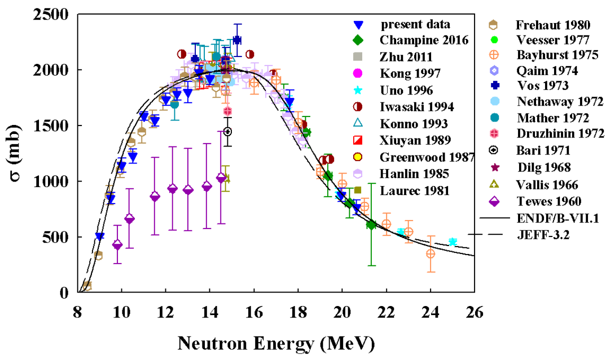

Figure 1.9: Experimental and literature data for the ^{169}Tm(n,2n)^{168}Tm reaction cross section.

The cross section of the ^{169}Tm(n,3n)^{167}Tm reaction was calculated at three energies when the incident neutron energy was above the reaction's threshold. Our results for are plotted in Fig. 1.10. The data from this work agrees well with the literature at neutron energies of 20 and 20.6 MeV. As expected, when the cross section is increasing for the ^{169}Tm(n,3n)^{167}Tm reaction, the cross section of the ^{169}Tm(n,2n)^{168}Tm reaction at the corresponding energy is decreasing.

Our measurement at 17.6 MeV for the ^{169}Tm(n,3n)^{167}Tm reaction is slightly higher than expected compared to previous measurements. It is worth noting that most of the existing data for this cross section are 20 to 40 years old, and no previous measurements were made using both a mono-energetic neutron source reaction and HPGe detectors.

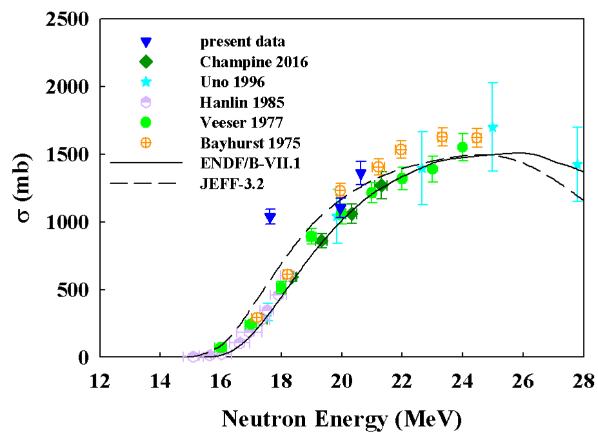

Figure 1.10: Experimental and literature data for ^{169}Tm(n,3n)^{167}Tm reaction cross section.

The present work provides comprehensive cross section data for the ^{169}Tm(n,2n)^{168}Tm reaction, as well as data for the ^{169}Tm(n,3n)^{167}Tm reaction. The results of these measurements provide the basis for investigating properties of the inertial confinement fusion plasmas from the deuterium-tritium capsules at NIF.

[Bhi14] M. Bhike and W. Tornow, Phys. Rev. C, **89**, 031602(R) (2014).

[Fre80] J. Frehaut *et al.*, *U.S. Report to the I.N.D.C.*, Technical Report 84, 1980.

[Vee77] L. Veeser *et al.*, Phys. Rev. C, **16**, 1792 (1977).

1.5 Enge Feedback System

C.M. Seed, *Boston College, Chestnut Hill, MA*; R.L. Longland, *TUNL*

A beam-centering feedback system for the high resolution beam line has been developed to streamline beam tuning procedures. A combination of low-cost hardware and advanced accelerator control software is used to read beam diagnostics (beam pick-off slits) and detect off-center beam trajectories. Magnetic steerers can then automatically correct the beam path. The feedback system has been fully characterized using an equivalent system of LEDs and photocells, and beam-line tests are currently underway.

Meaningful measurements taken using an accelerator require the particle beam to hit a chosen target in a well-defined position. This position is critical for high resolution charged-particle spectroscopy measurements, where the beam spot must be within a millimeter of the target center. To ensure that the beam hits the target correctly, a steering system exists. Diagnostic slits along the beam path measure the trajectory of the beam, and magnetic steerers are used to correct the beam path, thus centering the beam. These steerers are manually adjusted to tune the beam at each run so that as much beam as possible hits the target. In addition to these steering systems, quadrupole magnets are used to focus the beam. Unfortunately, if the beam is not well centered along the optical axis of the beam-line, these quarupoles tend to adversely steer the beam when they are adjusted.

For measurements using the high resolution beam-line, the beam must travel through two ninety degree turns before traveling to the target chamber, where the nuclear reaction takes place. This path requires several steerers and quardupoles to ensure transmission to the target chamber. Tuning the beam along this beam-line is a time consuming endeavor, requiring skilled operators. This is especially true for low-energy α-particle beams. A set of three, closely packed steerers are used in the final portion of the Enge beam-line to ensure that the beam stays well centered on the target. These steerers were designed to be used with a hardware feedback system, which automatically corrects drifts in the beam trajectory, thus aiding in beam tuning. Unfortunately, one of those feedback systems is no longer functional. The hardware required to restore that feedback capability is cost-prohibitive, so a low-cost alternative is desirable. It is hoped that a software feedback system will provide a low-cost alternative, decreasing some of the tuning difficulty because fewer controls need to be adjusted manually.

The Enge feedback system discussed here uses both low-cost hardware and advanced accelerator control software to process information from the slits and then control magnetic steerers to correct the beam path. The hardware includes an Arduino and a Raspberry Pi, while the software components primarily include the Experimental Physics and Industrial Control System (EPICS) [Dal94] with some Arduino programming [Jem13]. The Arduino programming allows the Arduino to act as an input/output controller that can be controlled by the outside program EPICS. EPICS contains the feedback protocol and commands, sending them to the Arduino. The software is designed to first read Arduino inputs (voltages from the slits that correspond to current balance) and then, based on a set point specified by the user, send a control voltage via the Arduino to the steerers. The Raspberry Pi was used to connect the feedback system to TUNL control network, allowing flexible remote control. A graphical user interface was designed so a user can (i) monitor the voltage readings from the slits and to the steerers; (ii) toggle feedback on and off; (iii) control the steerer currents independently in manual control mode; (iv) control the set point for the slits; and (v) control the feedback parameters to optimize the feedback loop.

Initially, the feedback system was built and designed using an LED and photocell in place of the steerer and slit. The photocell resistance changes according to the light intensity falling on it's surface, making it a good electrical analog of a beam slit. The convenience of the smaller scale accelerated software development and testing time. Figure 1.11 shows successful LED feedback. These tests confirm that the feedback system works and is effective in keeping the photocell close to the set point with minimal drift. Following this development stage, analog voltage outputs were added using a pair of digital-to-analog converters (DACs).

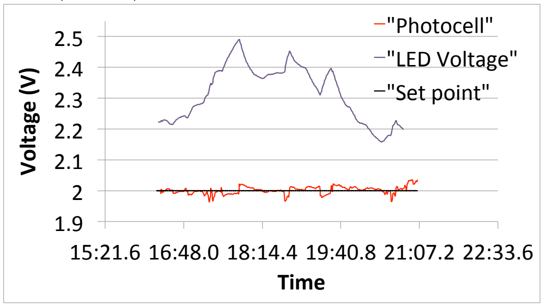

Figure 1.11: LED Feedback test showing how the photocell voltage was kept close to the set point with minimal error. The set point is 2 V.

Once the feedback system was built and proven to be working with the LED, it was adjusted to work for the beam. These adjustments include having two feedback loops in the program, one for the horizontal slits and steerers and one for the vertical slits and steerers. The DAC chips allow control voltages for the steerers. Additional adjustments are necessary because both the slits and the steerers operate on voltage ranges outside of the Arduino voltage range of 0 to 5 V. The steerers control-output circuit includes an active summing operational amplifier (op-amp) to scale the Arduino's output range of 0 to 5 V to span the range from -6 to 6 V. The circuit for the slit is similarly designed to convert the -5 to 5 V slit-balance signal to the 0 to 5 V range of the Arduino. A buffer op-amp prevents current flow to the slit-current amplifier, although this circuit is still under development.

The feedback system has been tested briefly under beam conditions using the high-energy slits prior to the 20-70 switching magnet at TUNL. A synthetic beam was used to determine how the steerers react and calibrate the fine control. Steerer control is effective. Unfortunately, full active feedback control could not be tested, because of difficulties with the Tandem accelerator charging chains. Only ten minutes of beam time were available for testing. However, we determined that the feedback system did work in adjusting the beam to the set point, but there is a drift from the set point by the beam, as shown in Fig. 1.12. Most likely, the cause of this drift is poorly tuned feedback parameters, but we were unable to test the system further due to the short amount of usable beam time. Poor voltage stabilization in the Tandem accelerator may also explain these issues. Further testing is required to fully characterize the feedback system.

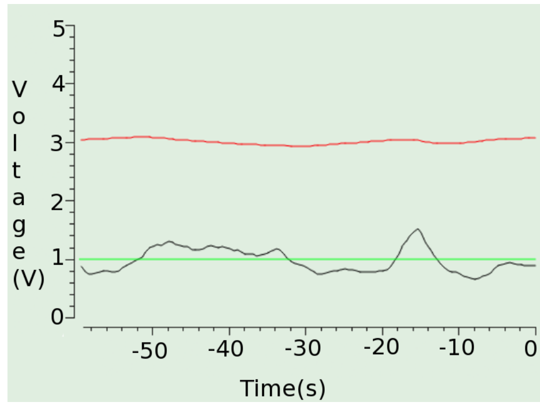

Figure 1.12: (Color online) Beam Feedback test. Red (highest line) is voltage to the steerer, black shows slit input, and green (flat line) shows the set point

Future work for this project includes the completion of the slit circuit to cover its full range, as well as further testing of the feedback system on the beam. If further testing proves the feedback system to be effective at centering the beam with acceptably small drift, then the feedback system can be integrated into the beam line steering system. The circuits required to connect the various pieces can also be constructed on a chip rather than a breadboard. Application of the feedback system to other steerers along the beam line would, if desired, be possible and fairly simple.

[Dal94] L. R. Dalesio *et al.*, Nucl. Instrum. Methods A, **352**, 179 (1994).

[Jem13] P. R. Jemian, *cmd_response*, 2013, `http://prjemian.github.io/cmd\_response/index.html`.

1.6 3D Printing of Radiation Detectors

A.N. Zawada, *Case Western Reserve University, Cleveland, OH*; P.S. Barbeau, *TUNL*

We are studying the capability of modern 3D printers to produce custom shaped scintillating detectors. We successfully created rectangular prints of the plastic scintillator polyvinyl toluene (PVT). Using a photo-multiplier tube and a ^{133}Ba source, we found that the fluorescence survived the printing process and the printed material was still scintillating. Further testing showed that the printed material has lower energy resolution than the raw material but is still able to detect the energies of important interactions.

Wavelength shifting and scintillating materials are an important part of many particle detection devices. However, forming them into specific shapes can be cost-prohibitive and has therefore limited the ways they are used. The ability to 3D print any desired shape from the variety of plastic materials available could open up many possibilities for how detection devices are built. Throughout the summer we worked to produce custom 3D printed scintillating pieces and ran tests to compare 3D printed polyvinyl toluene (PVT) to the raw material.

To produce the filament that would be used in the printer, we purchased a Noztek Pro extruder. Blocks of PVT were shaved down and fed into the top of the extruder where the material was melted down and pushed out of the nozzle to produce a 2.85 mm filament. Once the filament was formed, it was fed into the printer and rectangles of dimensions 27x25x5 mm were printed. Settings on the printer such as speed and layer height were adjusted to produce the highest quality and clearest prints. See Fig. 1.13.

The first test we ran on the printed sample was to determine if the fluorescence survived the extrusion and printing processes. A photomultiplier tube (PMT) and ^{133}Ba source were placed in a dark box, and two runs of thirty minutes each were taken, one when the printed scintillator was placed on the PMT and one when the scintillator was not in the box. There were roughly eleven times more events recorded when the scintillator was on the PMT, and therefore we can conclude that the fluorescence survived and the material was still scintillating.

The next step was to characterize the properties of the printed scintillators by comparing them to a piece of raw material of the same size. A 15 μC ^{22}Na source was placed in the dark box and the waveforms of events were recorded for thirty minutes. This was done twice, once with the raw and one with the printed material.

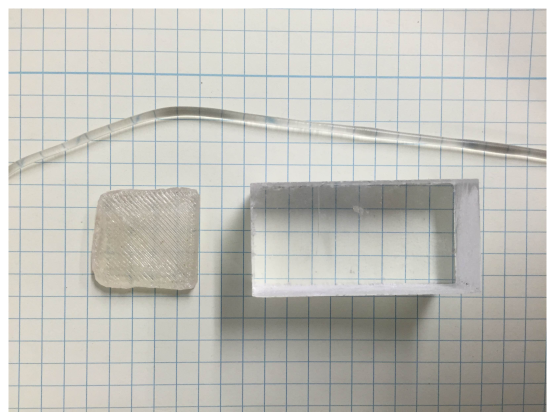

Figure 1.13: A block of raw PVT (lower right) is shaved down and extruded into a 2.85 mm filament (top) which is fed into the 3D printer to produce a rectangular piece (lower left).

Using a code written in ROOT, the waveforms were integrated and a histogram was generated. Since the integral of these waveforms is proportional to energy, this histogram is a scaled version of the energy spectrum of ^{22}Na. The histograms are shown in Figs. 1.14 and 1.15. Sodium has two decay populations. The first population is from a β^+ decay where a positron and a neutrino are emitted, leaving an excited daughter nucleus. The positron almost immediately annihilates with an electron to produce two γ rays with energies of 511 keV. The second decay interaction is the de-excitation of the daughter nucleus, which produces a γ ray with an energy of 1274 keV.

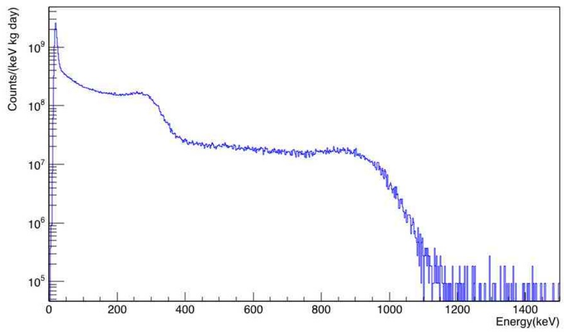

Figure 1.14: ^{22}**Na energy spectrum using raw PVT scintillating material. There are two Compton shelves corresponding to the two decay populations of sodium.**

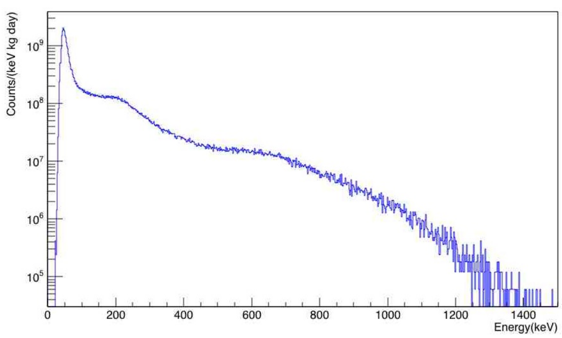

Figure 1.15: ^{22}**Na energy spectrum using printed PVT scintillating material. Two Compton shelves are shown, but with lower energy resolution.**

Our samples are too small for photoelectric absorption to occur, so the γ rays rarely deposit their entire energy onto an electron. Instead, a majority of the γ rays undergo Compton scattering, and the Compton shelves resulting from these interactions can be seen in the energy spectra. The edge of the shelf corresponds to the maximum energy deposition, which occurs when the γ ray deflects off of the electron at an angle of 180°. The energy of the electron following this interaction is given by the equation [Kno10]

$$E_{e^-} = h\mu \frac{2h\mu/m_0c^2}{1 + 2h\mu/m_0c^2}, \tag{1.2}$$

where m_0c^2 is the electron energy (511 keV) and hμ is the energy of the γ ray. Each graph displays two Compton edges, and using Eq. 1, it is possible to determine the corresponding energies of these edges. The first Compton edge is due to the electron-positron annihilation and appears at 340.7 keV, and the second Compton edge comes from the de-excitation of the daughter nucleus, which appears at 1061 keV. Since the electron-positron annihilation has a shorter half-life, it has a more counts than the de-excitation decay.

By comparing the two graphs, we can see that the printed scintillator has a lower energy resolution than the raw material. Intuitively this makes sense since the printed material went through more abuse than the raw material. Using a high precision camera, we took images in a dark box of the two pieces and saw that the printed scintillator was glowing, even without the presence of a radioactive source, as shown in the left panel of Fig. 1.16. One explanation for this is that the 3D printer had previously been used to print glow-in-the-dark material, and the scintillating filament had been contaminated. After cleaning the printer nozzle in an acetone bath, printing a new scintillating piece, and taking another image, we saw that the piece was no longer glowing, as seen in the right panel of Fig. 1.16.

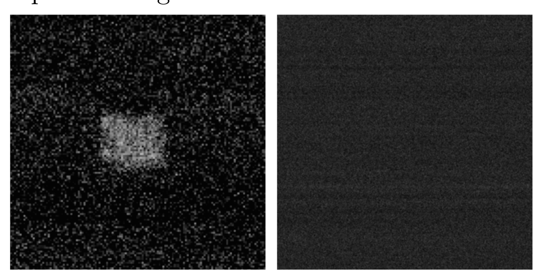

Figure 1.16: Printed material from unclean nozzle (left), printed material from clean nozzle (right).

In the future, printed pieces from the clean nozzle should be tested using the PMT and ^{22}Na source to determine if the energy resolution can be improved. Purchasing a new and higher quality 3D printer would be a good investment for a material that is especially sensitive to contamination. The next steps for this project include printing larger pieces that would realistically be used in particle detectors and running tests to determine if the size of the pieces is related to the energy resolution.

[Kno10] G. F. Knoll, *Radiation Detection and Measurement*, John Wiley & Sons, Inc., Hoboken, NJ, 4^{th} edition, 2010.

1.7 Nuclear Data Evaluation for ^{15}F

Q.V. Truong, *Lenoir-Rhyne University, Hickory, NC*; J.H. Kelley, G.C. Sheu, *TUNL*

We have reviewed all available literature on ^{15}F to determine the most accurate experimental energy levels and produce recommended values for inclusion in the Evaluated Nuclear Structure Data File. In addition, recently published experimental articles on other nuclides have been compiled for the database Experimental Unevaluated Nuclear Data List.

The nuclear data group at TUNL is responsible for producing evaluations in the nuclear mass region $A = 2$ to 20. Our activities primarily involve studying literature articles and producing recommended values for inclusion in two databases: Experimental Unevaluated Nuclear Data List (XUNDL) and Evaluated Nuclear Structure Data File (ENSDF). Nuclear data evaluation is necessary to produce recommended values for use in nuclear physics research and relevant applied technologies such as radioactive dating, nuclear reactor physics, nuclear medicine, and homeland security.

Our project focused on compiling the reported resonance energy values of ^{15}F and producing recommended values to include in an online database at TUNL. Our ultimate goal is to adopt energy levels that can be included in the ENSDF database at the National Nuclear Data Center (NNDC) at Brookhaven National Laboratory.

To accomplish these goals, we reviewed all available experimental articles on ^{15}F compiled using the Nuclear Science References database from the NNDC. Each article was carefully examined to make sure that the excitation energy of the peak was actually measured, not compiled from other sources, and that the value was reliable. Discussions and comments made by the authors were also reviewed for inclusion in the evaluation report.

The data-averaging software used was the Visual Averaging Library. We used the software to produce a recommended average value for each energy level by comparing eight different averaging techniques: unweighted average, weighted average, limitation of relative statistical weights, normalization residuals, Rajeval technique, method of best representation, bootstrap, and Mandel-Paule. The unweighted average is fairly intuitive, but this method is inappropriate when the values have different uncertainties.

Giving some values more weight based on their relative credibility and accuracy is recommended. Therefore, the weighted average is the preferred method for data evaluation. The weighted average gives the most precise values more weight in the averaging. This technique works very well if the data are consistent, as was the case for most of the ^{15}F energy levels other than the ground state.

Sometimes, however, values do not agree well, and other methods must be used. The next-most-reliable method is the limitation of relative statistical weights, which manipulates the weights such that no single value carries more than fifty percent of the weight. The thought is that if one value is very much more precise than the others, it is possible that its uncertainty has been greatly underestimated and its weight should be limited.

When there is inconsistency in the data, the method of best representation is often recommended. It uses the measurements to construct a mean probability density for the data set. This method would give a more realistic uncertainty, would be robust to outliers if present, and would be consistent under various representations of the same quantity, as was the case for the ground state of ^{15}F.

The rest of the averaging methods have similar ways of working with the assumption that if the values have poor agreement, they must be inaccurate. However, the weighted average, the limitation of relative statistical weights, and the method of best representation are the most commonly used. In addition, averaging methods can be compared using a chi-square test.

These methods can produce a very low uncertainty value that is lower than the lowest uncertainty from the individual measurements. In that case we chose to adopt the lowest individual uncertainty.

As is often the case with data sets, the excitation energy values sometimes included outliers. The averaging software picks out outliers (values that deviate

Table 1.5: Adopted energy levels and resonance widths for ^{15}F

E(level) (keV)	J_π	Γ (keV)	$E(p+^{14}\mathrm{O})_{\mathrm{cm}}$ (keV)
0	1/2+	600 (20)	1.28×10^3 (4)
1.52×10^3 (5)	5/2+	300 (13)	2798 (24)
3.48×10^3 (4)	1/2−	36 (15)	4757 (12)
5.1×10^3 (2)	(3/2−, 5/2−)	200 (200)	6.4×10^3 (2)
6.5×10^3 (2)	(3/2+,5/2+)	400 (400)	7.8×10^3 (2)

from the mean) using Chauvenet's Criterion, without taking uncertainties into account. This means that it is as possible for inaccurate values to be targeted, as it is for the most-reliable ones. Therefore, it was important to take the outliers into account, but to use caution before dismissing anything.

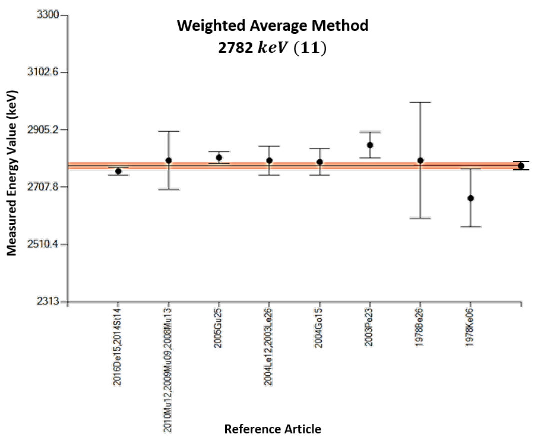

Figure 1.17: First excited state energy values for ^{15}F with their weighted average.

The example of the first excited state energy values of ^{15}F is shown in Fig. 1.17. This is a fairly intuitive example, where all of the values agree well, and the weighted average overlaps all the values. The chi-square value of the weighted average is 1.16, much lower than the critical chi-square of 2.01. Therefore, we adopted the weighted average and adjusted the uncertainty to match that of the measurement with the lowest uncertainty.

The case of the ground state energy values is quite different, as shown in Fig. 1.18. Here the values disagree significantly, and the uncertainties for half of them lie well outside the uncertainty associated with the weighted average. The chi-square value of 2.60 is above the critical chi-square of 2.01. Before adopting a recommended value for the ground state, it was important to review the articles and examine different averaging methods. This led us to adopt the average value shown in Table 1.5.

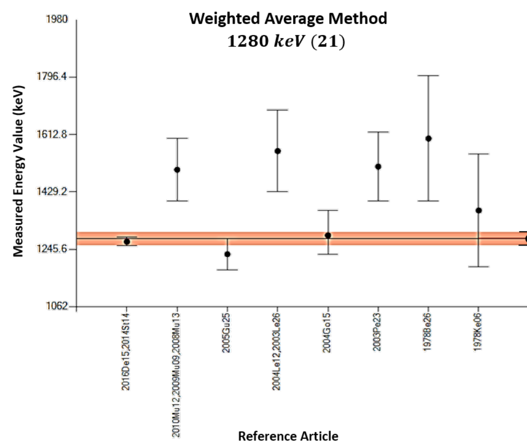

Figure 1.18: Ground state energy value for ^{15}F plotted alongside their weighted average.

In conclusion, we have reviewed all available literature on ^{15}F to determine the most accurate experimental energy levels and nuclear structure parameters. The recommended values shown in Table 1.5 are for use in the XUNDL database at TUNL and the ENSDF database at Brookhaven National Laboratory. We have also compiled recent published experimental articles on different light nuclides that are available for future reference in XUNDL.

1.8 Identification of the Neutral Current Interaction of Neutrinos in Liquid Argon Detectors

A.J. Roeth, *University of Oklahoma, Norman, OK*; K. Scholberg, *Duke University, Durham, NC*

The neutral current interaction can occur between any flavor of neutrino and argon. In this interaction, the neutrino excites the argon nucleus, which then decays via a γ ray of approximately 10 MeV. In order to identify this interaction in liquid argon detectors, these γ rays must be differentiated from other particles of similar energies. Electrons and γ rays of 10 MeV were simulated and reconstructed using the LArSoft software package models of the Deep Underground Neutrino Experiment's liquid argon detector. The reconstructed products were analyzed spatially to study the differentiation of γ rays from electrons and the ability to identify this neutral current interaction.

When a star collapses, it explodes in what is called a supernova. About 99% of its binding energy is released in the form of neutrinos, which are leptons with masses much smaller than any other standard-model particle. The flavor and energy spectra of neutrinos over time could provide insight into the physics of the processes of supernovae and the properties of neutrinos [Sch12].

Within a few tens of milliseconds from the start of a supernova, a burst of electron neutrinos is released [Sch12]. Because there is a major interaction channel for electron neutrinos with liquid argon [Rag86], liquid argon detectors are more sensitive to electron neutrinos, and therefore more useful for detecting supernovae, than other types of detectors, such as water detectors [Rag86]. An experiment that will utilize a liquid argon neutrino detector is the Deep Underground Neutrino Experiment (DUNE), which is currently in the design stage.

The neutral current interaction occurs between all flavors of neutrino and liquid argon, so it has potential to be used to calculate the total flux of all flavors [Hay16]. In this interaction, a neutrino interacts with the argon nucleus via a neutral Z boson, exciting the nucleus, which then decays via a γ ray of approximately 10 MeV [Hay16]. In order to identify the neutral current interaction, the 10 MeV γ ray must be identified, and this involves differentiating it from electrons of similar energies produced in other neutrino interaction channels.

In a liquid argon detector, electrons and γ rays lose energy in different ways. Electrons are charged particles, so as they travel through the liquid argon, they ionize it, losing their energy continuously. They are also capable of producing bremsstrahlung radiation. However, γ rays lose energy through pair production, Compton scattering, and the photoelectric effect. Thus γ rays are detected via the charged particles, electrons and positrons, that they create or interact with. These create tracks of ionization, and the ionized electrons collected on a wire plane are the detector's signal. Therefore, one expects that electrons and γ rays would produce differentiable patterns of charged particle tracks in the LArSoft liquid argon detector model. Because γ rays lose energy in separate processes rather than one continuous track, 10 MeV γ events were predicted to produce tracks that were more numerous and farther apart than those of 10 MeV electron events.

The LArSoft software package was used to simulate and reconstruct particles in a model of DUNE's liquid argon detector. Reconstruction was previously optimized for higher energy events, so in order to be able to identify the neutral current interaction, reconstruction had to be adjusted to make it capable of reconstructing 10 MeV γ rays and electrons. Reconstruction in LArSoft consists of multiple steps: finding hits of electrons on the wire plane, grouping the hits into clusters, and then constructing 3-dimensional (3D) tracks, one for each charged particle in an event. The tracks are made up of 3D space points. Reconstruction was improved by working with three DUNE collaborators to find the best cluster-finding algorithm for low energy events. We then modified the tracking algorithm to be compatible with the cluster-finding algoithm and changed the parameters in the track-finding algorithm. Figure 1.19 shows how much reconstruction efficiency of low energy electrons was improved. Efficiency is defined as the ability to reconstruct at least one space point of the 3D track.

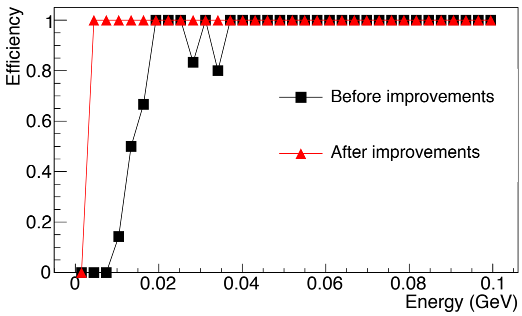

Figure 1.19: Reconstruction efficiency vs. electron energy.

A LArSoft analysis module was written to graph information about the reconstructed tracks. Electrons and γ rays with energies of 10 MeV were generated, simulated, and reconstructed in LArSoft, and then the analysis module was run on the resulting reconstructed information. The analysis module graphed the number of tracks, the mean distance (defined as the average distance between all possible pairs of space points), and the maximum distance (defined as the maximum distance between all possible pairs of space points).

Figure 1.20 shows the number of tracks for 10 MeV electrons and γ rays. Among the events where a track could be reconstructed, there were more γ-ray events than electron events with two or three tracks, and more electron events with only one track. Figure 1.21 shows the mean distance for 10 MeV electrons and γ rays, and Fig. 1.22 shows the maximum distance. There were more γ events than electron events with larger mean distances and larger maximum distances.

The number of tracks, mean distance, and maximum distance cannot be used alone to identify γ rays, but because they are different for γ rays and electrons, they could be useful to accomplish this. Future work on this project will consist of analyzing the tracks of γ-ray and electron events in more ways and using the information to develop a neutral-current-interaction identification algorithm.

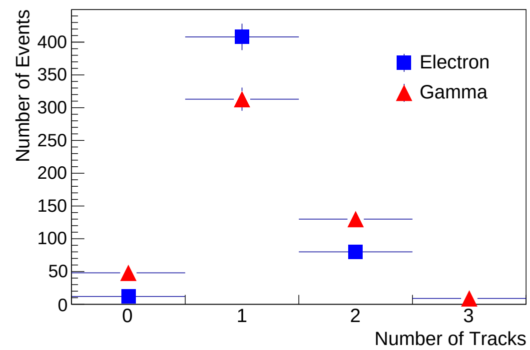

Figure 1.20: Number of tracks for 10 MeV electrons and γ rays.

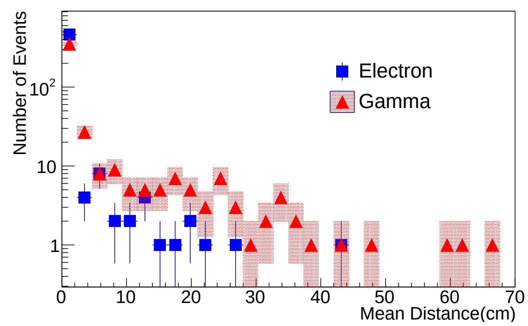

Figure 1.21: Average distance between all space points for each event for 10 MeV electrons and γ rays.

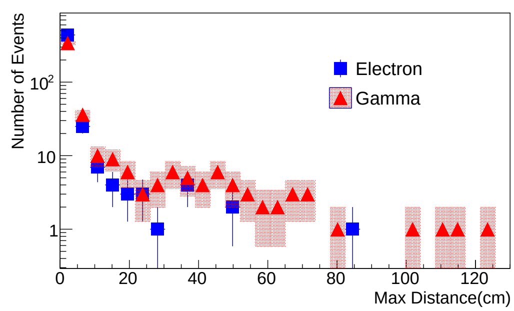

Figure 1.22: Maximum distance between all space points for each event for 10 MeV electrons and γ rays.

[Hay16] *Private correspondence with Dr. Anna Hayes.*, 2016.

[Rag86] R. Raghavan, Phys. Rev. D, **34**, 2088 (1986).

[Sch12] K. Scholberg, Ann. Rev. Nucl. Part. Sci., **62**, 81 (2012).

Research Based at CERN

Chapter 2

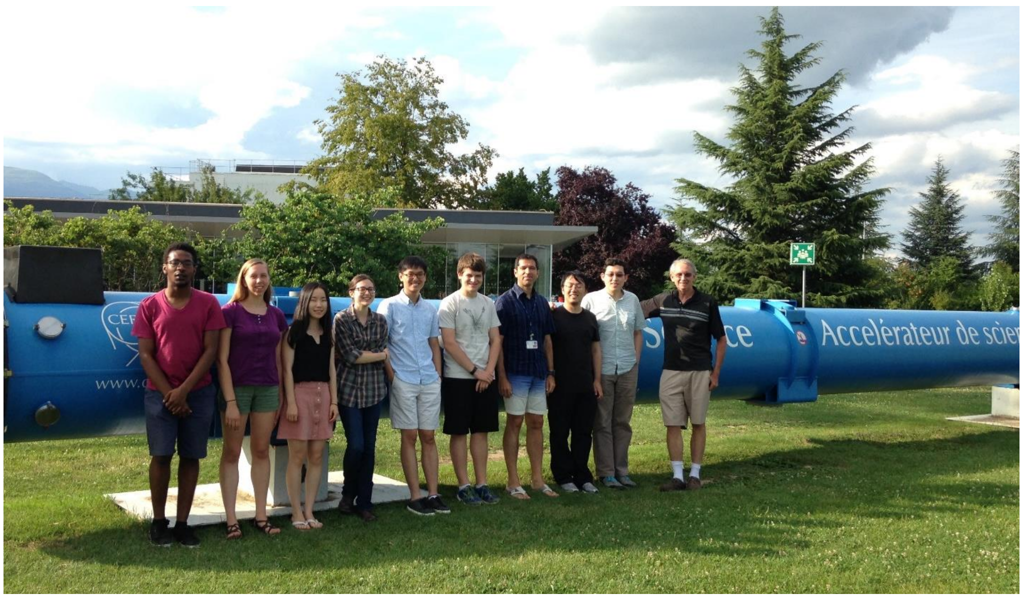

2.1 First Measurement of $Z+\gamma$ Production in 13-TeV Proton-Proton Collisions

E.M. Stump, *Williams College, Williamstown, MA*; A.T. Goshaw, A. Bocci, *Duke University, Durham, NC*

This initial study of $Z(\mu^+\mu^-)\gamma$ events from proton-proton collisions at 13 TeV compares these new data to Standard-Model (SM) predictions and searches for evidence of beyond-the-Standard-Model (BSM) processes. It was found that the data generally agree with SM predictions, with no evidence for BSM physics.

In Run II, the Large Hadron Collider (LHC) has begun to produce proton-proton (pp) collisions with an unprecedented center-of-mass energy of 13 TeV. With this significant energy increase from the previous 8 TeV collisions, scientists at the LHC seek to measure processes predicted from the Standard Model (SM), as well as search for evidence of new physics beyond the Standard Model (BSM).

In this study, events producing $Z\gamma$, with $Z \to \mu^+\mu^-$ were examined. Although this decay channel is fairly rare, it was chosen because the background associated with the decay channel is very small. The expected production process based on SM predictions is $q\bar{q} \to Z(\mu^+\mu^-)\gamma$. Two additional hypothetical BSM decay processes were also considered. The first (see Fig. 2.1) is the radiation of a photon by the Z. Since Z is a neutral particle, under the SM assumption that the Z is an elementary particle, this process should never occur. However, if the Z were a composite particle, with charged components, then electromagnetic radiation could occur. The second additional decay considered (see Fig. 2.2) is the production of a high-mass X boson in the initial $q\bar{q}$ interaction, with $X \to Z(\mu^+\mu^-)\gamma$.

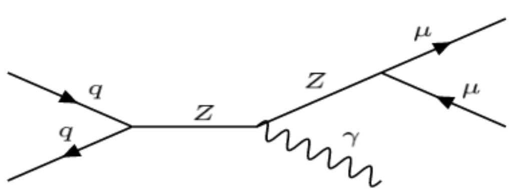

Figure 2.1: Feynman diagram showing the radiation of a photon by a Z boson.

The data set analyzed in this study consisted of Run-II 13-TeV pp collisions recorded in the ATLAS detector and triggered on a high-momentum muon. The integrated luminosity represented by these data was 4.3 fb^{-1}, and the triggered data set contained 757,657 events. Cuts were applied to this initial data set based on a similar analysis of $q\bar{q} \to Z(\mu^+\mu^-)\gamma$ in 8-TeV data by the ATLAS collaboration [ATL16]. These cuts removed events in which the photon or muons were detected near the limits of the detector and selected for events containing two muons and a photon such that these particles had sufficiently high transverse momenta to be potentially characteristic of the $q\bar{q} \to Z(\mu^+\mu^-)\gamma$ decay process.

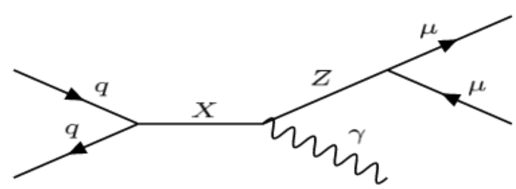

Figure 2.2: Feynman diagram showing a quark-antiquark pair producing and X boson, which then decays to $Z(\mu^+\mu^-)\gamma$.

Rudimentary selections were also made to exclude events with fake jets. Since photons, like quarks and gluons, are detected by energy deposition in a calorimeter, jets produced by these quarks and gluons are often improperly reconstructed as photons, resulting in the phenomenon of fake jets. These fake jets create an unfavorable background to the signal of interest, and this removal, while fairly effective, is nevertheless unable to identify all fake jets.

After these initial cuts, 5539 events of interest remained in the data sample. A final cut was made to select for events in which the combined invariant mass of the two muons was between 80 and 100 GeV, in order to isolate true $Z \to \mu^+\mu^-$ decays from background resulting from $Z \to \mu^+\mu^-\gamma$ decays.

With these cuts implemented, the remaining events were compared to simulated $q\bar{q} \to Z\gamma$ events based on SM predictions, with the same selection cuts applied. Three parameters were considered for both the photon and the muons: the transverse energy of the particle, the pseudorapidity, and the azimuthal angle. The distributions of these parameters for the simulated and actual data were generally in agreement with one another (see, for example, Fig. 2.3).

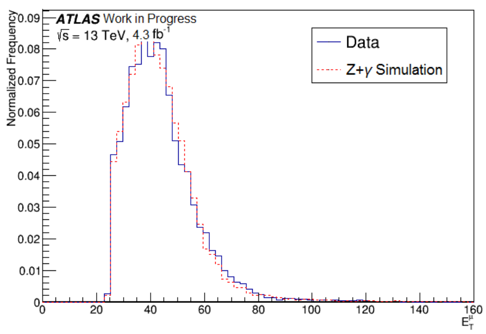

Figure 2.3: Comparison of muon transverse-energy distribution for actual and simulated data events.

However, the distributions of photon transverse energy for the actual data and simulated data show noticeable disagreement (see Fig. 2.4). In particular, the distribution for actual data suggests an excess of photons at low transverse energy, as compared to the expected counts. This excess at low energies is consistent with the decaying-exponential distribution of jet transverse momentum, suggesting that the inconsistency between the actual data and simulated data results from an incomplete removal of fake jets from the data sample. For further analysis of this data sample, the fake-jet-removal process would need to be improved to ensure that the sample consists purely of $Z+\gamma$ events and contains no $Z+$jet events.

Parameters that might provide evidence for the presence of BSM physics were also considered. In looking for evidence of an X boson, the distribution of the invariant mass of $\mu^+\mu^-\gamma$ was examined. If an X had been produced, the distribution of this invariant mass would include two peaks, one slightly above 91 GeV, resulting from SM production of Z and a relatively low-energy photon, and one at a much higher energy, corresponding to the mass of the X. However, an inspection of this distribution revealed no such peak at higher energies, providing no evidence for the production of an X boson.

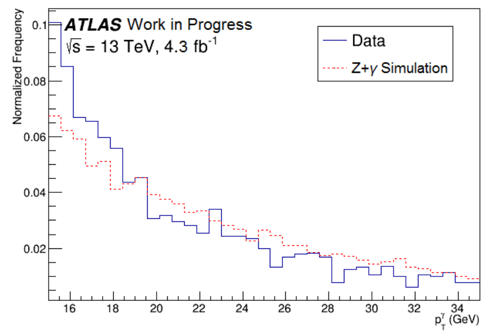

Figure 2.4: Comparison of photon transverse-energy distribution for actual and simulated data events.

In looking for evidence of a composite Z boson, the distribution of the photon transverse energy was examined. In order to find differences between the actual-data distribution and the simulated-data distribution that would be characteristic of photon radiation by the Z, the distribution was inspected for the presence of an excess of high-energy photons. The highest photon transverse energy observed was near 400 GeV, with no other values near that same higher energy. Thus, this distribution provided no evidence for the existence of a composite Z boson.

This initial study of $Z(\mu^+\mu^-)\gamma$ production at 13 TeV has shown reasonably good agreement with SM predictions but unfortunately has not revealed any evidence for BSM physics. Further study of this decay process at 13 TeV will hopefully provide constraints on the BSM physics that might be found on this energy scale.

[ATL16] The ATLAS Collaboration, Phys. Rev. D, **93**, 112002 (2016).

2.2 Comparison of Fixed-R and Variable-R Jet Reclustering Using a 750 GeV Resonance

H.M. Glaser, *Virginia Tech, Blacksburg, VA*; A. Arce, *Duke University*

The jet clustering algorithm using a variable R parameter during sequential recombination has already been tested against the traditional fixed-R_0 algorithm for certain reactions at TeV-scale jet transverse momenta. In the present work we test it in the energy range of hundreds of GeV for an X $\rightarrow$ Z + γ reaction, which results in a different polarization distribution than do the previous test reactions. Here, we compare the results of using anti-k_T fixed-R and variable-R reclustering on a set of simulated 0.4 R H750 $\rightarrow$ Z + γ jets. Results indicate a slight improvement in QCD background suppression and more accurate mass reconstruction with the variable-R approach.

Jets are clusters of detector signatures stemming from the same parent quark or gluon, as determined by a clustering algorithm. The most commonly used algorithms use the process of sequential recombination. For each pair of input particles i and j, two quantities are calculated:

$$d_{ij} = \min(p_{Ti}^{2n}, p_{Tj}^{2n})\Delta R_{ij}^2, \quad \text{and} \tag{2.1}$$
$$d_{iB} = p_{Ti}^{2n} R_0^2, \tag{2.2}$$

where p_T is the transverse momentum, ΔR_{ij} is the geometrical distance between momentum 4-vectors of the two particles, and n and R_0 are chosen parameters. If the smallest of all d_{ij} and d_{iB} is a d_{ij}, then the two 4-vectors are combined into one and the process repeats. If the smallest is a d_{iB}, then their sum becomes a final jet. This ends when specified terminating conditions are fulfilled.

Different algorithms vary in their choice of n, but the parameter R_0 has always been held fixed, even though this is not an accurate model. When a relativistic particle decays, its decay products are collimated in the direction of its motion relative to the laboratory frame at a rate proportional to the mass of the parent particle and inversely proportional to its energy. Therefore, it is more logical to employ a variable R_0 parameter that mimics this relationship. This is the defining feature of the new variable-R algorithm [APP16], in which R_0 is replaced by the function

$$R_{\text{eff}} = \frac{\rho}{p_{Ti}}, \tag{2.3}$$

with ρ a parameter that sets the rate of change of R_{eff} with p_T.

The goal of this project was to determine whether fixed-R anti-k_T or variable-R reclustering is more effective in reconstructing a 750 GeV resonance for the reaction H750 $\rightarrow$ Z + γ with Z decaying into two quarks. This choice was made in part due to the interest raised by what appeared to be a 750 GeV di-photon resonance emerging in the data collected by both the ATLAS and CMS collaborations in late 2015. Although this fluctuation has since disappeared, the present results are useful in exploring the potential advantages of the variable-R algorithm.

Previous tests of this algorithm have been done in the TeV energy range for the reactions $t\bar{t} \rightarrow (W^+b)(W^-b)$, $hh \rightarrow (b\bar{b})(b\bar{b})$, and $WW \rightarrow (q\bar{q})(q\bar{q})$. The results showed improvement over the fixed-R algorithm, although the effects diminished with lower jet p_T. Similar investigations at lower energies are motivated by the fact that different reactions result in different polarization distributions—and therefore different angular distributions—of the end products.

For the present analysis, EventLoop was used as an interface between an xAOD file of 30,000 simulated H750 $\rightarrow$ Z + γ events and ROOT. The anti-k_T and variable-R algorithms were provided by the JetMET working group's JetReclustering package [Sta]. The quantity ρ was set to the mass m_Z of the Z boson, or about 91 GeV. In each approach, 0.4 R jets were reclustered, and the results were compared for QCD background suppression, highest p_T jet invariant mass, and H750 invariant mass. In order to reduce noise, the mass of H750 was calculated using only the highest p_T jet and the highest p_T photon for each event. Jet substructure was also analyzed by measuring the N-subjettiness ratio τ_2/τ_1 and the $D2$

variable, but, as expected for reclustered jets, these were both approximately zero for both algorithms.

Figures 1 and 2 display the results for jet invariant mass. In both cases, the peak is close to the expected m_Z, but both the second peak, caused by incomplete capture of the jet, and the QCD background are reduced using a variable R.

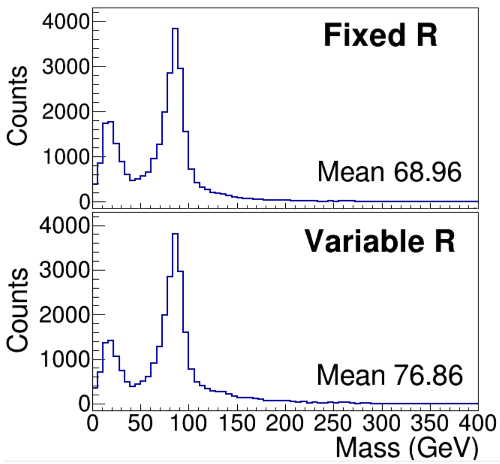

Figure 2.5: Highest p_T jet invariant-mass reconstruction.

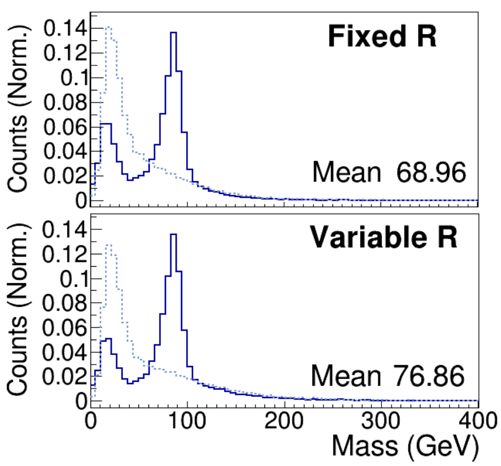

Figure 2.6: Highest p_T jet invariant-mass reconstruction with normalized QCD background.

Figures 3 and 4 show the reconstructed H750 mass. Although background suppression appears to be about equal for the two, the variable-R output is again slightly closer to the expected value, and the peak is more symmetric. Based on the present results, the variable-R approach appears to be a promising step forward for jet clustering algorithms and worth further exploration.

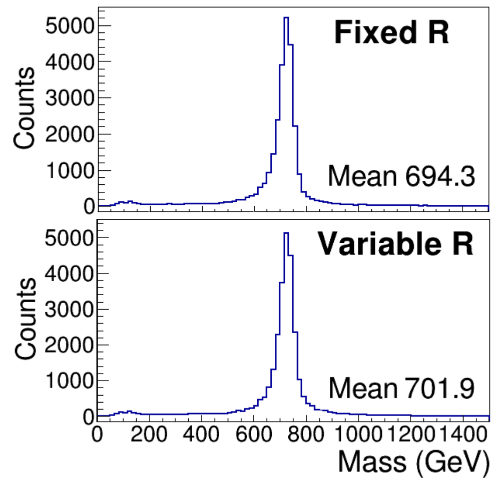

Figure 2.7: H750 mass reconstruction.

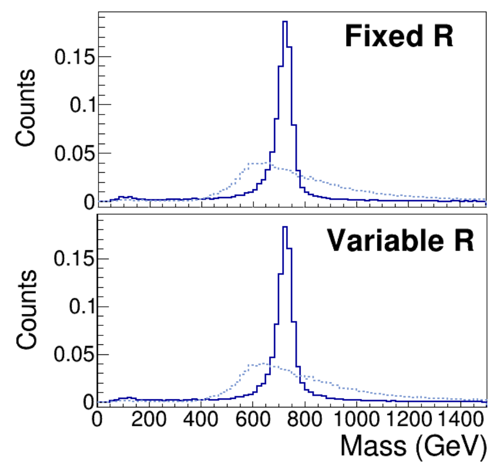

Figure 2.8: H750 mass reconstruction with normalized QCD background.

[APP16] ATL-PHYS-PUB-2016-013, *Boosted Object Tagging with Variable-*R *Jets in the ATLAS Detector*, Technical report, CERN, 2016, `https://cds.cern.ch/record/2199360`.

[Sta] G. Stark and J. Burr, *JetReclustering Package README.md*, `https://github.com/kratsg/JetReclustering`.

Index

Anthony, A.K., 2

Glaser, H.M., 21

Hobson, C.M., 4

Roeth, A.J., 16

Seed, C.M., 10
Soter, J., 8
Stump, E.M., 19

Truong, Q.V., 14

Wolff, M.S, 6

Zawada, A.N., 12